remote sensing

Article

Structure, Mechanisms, and Impacts of Nocturnal Downslope Wind Events in the Taklimakan Desert

Mohamed Elshora [1,2,3], Lian Su [4], Tianwen Wei [2,5] and Haiyun Xia [1,2,5,*]

[1] School of Earth and Space Sciences, University of Science and Technology of China, Hefei 230026, China; mohamedelshora@mail.ustc.edu.cn
[2] School of Atmospheric Physics, Nanjing University of Information Science and Technology, Nanjing 210044, China; twwei@nuist.edu.cn
[3] Department of Public Works Engineering, Faculty of Engineering, Tanta University, Tanta 31511, Egypt
[4] Institute of Optics and Electronics, Chinese Academy of Sciences, Chengdu 610207, China; kiwensu@mail.ustc.edu.cn
[5] State Key Laboratory of Climate System Prediction and Risk Management, Nanjing University of Information Science and Technology, Nanjing 210044, China
* Correspondence: hsia@ustc.edu.cn

Abstract

This study used reanalysis and lidar observations to investigate nocturnal downslope wind events in the Taklimakan desert, revealing their vertical structure, influencing factors, climatology, and impacts on boundary layer dynamics and dust emissions. 125 events were detected along the northern slope of the Kunlun Mountains, impacting Minfeng. Due to its weakness after onset, downslope flow is deflected horizontally when it encounters the opposing synoptic winds. The continued radiative cooling, dense air drainage, and adiabatic warming intensify downslope flow as the night progresses, causing it to gradually sink and overcome the opposing synoptic winds. Downslope wind events typically occur between an hour before and two hours after sunset, with the strongest occurring at or before sunset due to the longer period of radiative cooling and the coincidence with early evening instability conditions. Strong events occur under weak stability conditions as a stable atmosphere with a strong inversion layer can inhibit sinking motion. Most events, even the strongest ones, occur under dry conditions due to enhanced radiative cooling. Mechanical turbulence occurs when downslope flow hits the surface, whereas thermal turbulence occurs when warmer, downslope air weakens the lower atmosphere's temperature inversion. Downslope wind events significantly raise dust emissions in the Taklimakan desert.

Keywords: slope winds; nocturnal downslope flow; atmospheric boundary layer; dust emissions; Taklimakan desert; coherent Doppler wind lidar

Academic Editor: Dimitris Kaskaoutis

Received: 13 July 2025
Revised: 16 August 2025
Accepted: 25 August 2025
Published: 27 August 2025

Citation: Elshora, M.; Su, L.; Wei, T.; Xia, H. Structure, Mechanisms, and Impacts of Nocturnal Downslope Wind Events in the Taklimakan Desert. *Remote Sens.* **2025**, *17*, 2984. https://doi.org/10.3390/rs17172984

1. Introduction

The Taklimakan desert, which is the world's 2nd-largest shifting sand desert covering an area of 337,000 km^2 and dunes reaching a height of about 91 m, is a main source of dust aerosols in East Asia [1]. It is a part of the Tarim Basin in southwestern Xinjiang, Northwest China, and is surrounded by the Kunlun Mountains to the south, the Gobi Desert to the east, the Tianshan Mountains to the north, and the Pamir Mountains to the west, as shown in Figure 1. Due to severe winds, arid weather, and enormous volumes of dunes, Taklimakan desert dust storms are regular natural phenomena, especially in spring. Taklimakan desert dust aerosols can be lifted into the high atmosphere and carried vast distances eastward, affecting the air quality of numerous locations [2,3]. During dust events, particulate matter concentrations increase significantly, as demonstrated by Xie et al. [4] in Beijing and Liang et al. [5] in Taiwan. Zong et al. [6] also revealed that dust is predominant in the Taklimakan desert, with dust layers reaching a height of 4–5 km.

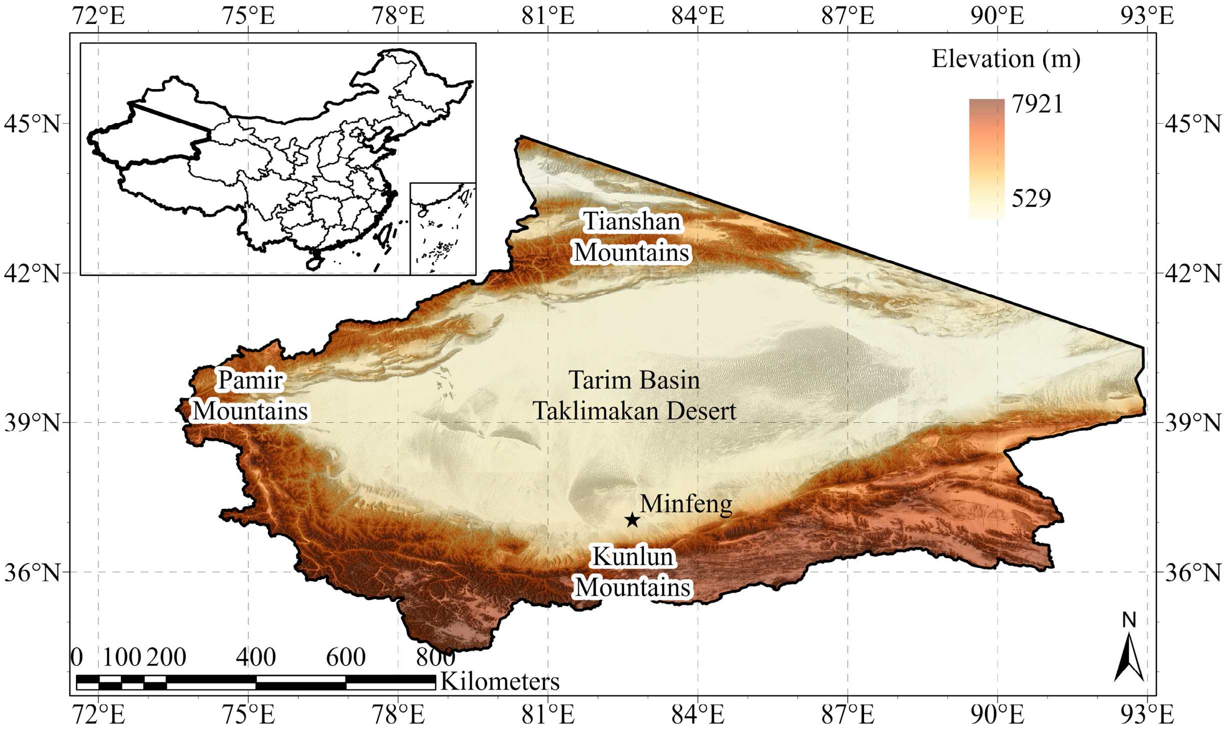

Figure 1. The study area and its topography.

Wind is the primary driver of dust aerosols, playing a crucial role in shaping arid and semi-arid environments. Diurnal mountain winds, also known as thermally driven slope winds, are common local winds in mountainous regions that occur due to the diurnal cycle of incoming solar radiation during the day and radiative loss during the night, which causes horizontal differences in temperature between the air above the heated or cooled slope and the air in the basin [7,8]. During the day, the sun heats the slope's surface, forcing the air above it to warm, become less dense, and rise, resulting in upslope (Anabatic) winds. During the night, the slope rapidly loses heat by radiative cooling, forcing the air above it to cool, get denser, and fall by gravity, resulting in downslope (katabatic) winds. The thermally driven slope winds are characterized by two daily transition phases: in the evening and morning. The evening transition from upslope to downslope occurs between late afternoon and early evening, shortly after sunset. It happens when outgoing longwave radiation surpasses incoming shortwave radiation, causing the surface to cool and triggering a downward sensible heat flux that removes heat from the air above the surface. The morning transition from downslope to upslope occurs in the early morning, shortly after sunrise. It happens when incoming solar radiation surpasses longwave radiation loss, breaking up the temperature inversion and transferring heat upward from the surface to the air above it [9–11]. The atmospheric boundary layer's thermal and dynamic structure is significantly influenced by the slope flows [12,13].

Nighttime katabatic winds are local phenomena, occurring on a smaller scale, such as a hill or a slope, and do not always require mountain peaks. The fundamental element is the cooling of air along a slope, which increases its density and causes it to flow downhill, driven by gravity [14]. Katabatic winds develop early after sunset, under clear skies and quiet synoptic conditions, at depths ranging from a few tens to a few hundred metres, within a developing temperature inversion, and with wind speeds increasing from the ground to 2–6 m s^{-1} before decreasing again from the jet to the top of the inversion [15–18]. They are weak and deep over gentle slopes [19], but strong and shallow over steep slopes [20]. Considering the whole mountain scale, the formation of a localized high-pressure system at mountain peaks throughout the night can also induce katabatic downslope winds. More rapid cooling of the air at the top of the mountain compared to that at lower elevations causes a pressure gradient, pushing the cold, dense air downhill. These local thermal pressure gradients are caused by differential cooling. The nightly downslope winds, which are generated by gravity and pressure gradient forces and have considerable impacts on the atmospheric boundary layer of large regions at the mountain's foot, are investigated in this paper. Arrillaga et al. [21] studied the locally produced, thermally driven downslope winds, considering their source, relationship to boundary-layer turbulence, and effect on the variability of CO_2 in the Guadarrama Mountains in the central Iberian Peninsula, Spain, during the summer of 2017. Wenta and Cassano [22] used observations from the Aerosonde unmanned aircraft system, numerical modelling, and the Antarctic Weather Station to investigate the effects of katabatic wind events over the Terra Nova Bay Polynya between 18 and 25 September 2012, on the atmospheric boundary layer and surface conditions.

While local temperature differences caused by nighttime surface cooling drive thermal downslope winds, large-scale weather patterns, especially synoptic pressure systems, drive synoptically forced downslope winds. The regulating mechanisms of the synoptically forced downslope winds include the interaction of synoptic flow with a topographic barrier that causes descending flow over its lee side [23]. The substantial cross-barrier flow is accompanied by condensation of moisture into clouds and precipitation on the windward slope and adiabatic warming on the leeward slope [24,25]. The synoptically forced downslope winds are not included in this paper; however, previous studies have examined them, such as Abatzoglou et al. [26], who studied them globally using reanalysis data from 1979 to 2018, as well as Shestakova et al. [27], who studied them in the Russian Arctic using reanalysis and observational data during the late 20th and early 21st centuries. Furthermore, Takimoto [28] investigated the downslope winds of Mount Rokko in Kobe City, Japan, utilizing wind and temperature observations collected between November 2017 and February 2018.

Previous research has demonstrated the role of northeasterly synoptic winds entering the Taklimakan desert through its eastern open in generating turbulence and dust storms. Elshora et al. [29], who analyzed a series of severe dust storms in the Taklimakan desert between 16 and 27 March 2022, found that northeasterly synoptic winds had a substantial role in the formation of these dust storms. However, researchers have not thoroughly examined the impacts of regular nighttime downslope wind events on atmospheric boundary layer characteristics and dust emissions. The existence of the Tianshan Mountains in the north, the Pamir Mountains in the west, and the Kunlun Mountains in the south causes it to receive frequent downslope wind events. With the majority of Taklimakan desert dust events occurring in its southern regions [30], specifically Minfeng City [31], this study focuses on detecting nighttime downslope wind events over the northern slope of the Kunlun Mountains, which have a substantial influence on Minfeng's atmospheric boundary layer. The Kunlun Mountains, which stretch from Tajikistan's Pamir Mountains to southern Xinjiang and Qinghai in China, are one of Asia's largest mountain ranges, covering more than 3000 km. The chain forms the northern boundary of the Tibetan Plateau south of the Tarim Basin, with a peak of 7167 m. This study thoroughly investigates nighttime downslope wind events over the northern slope of the Kunlun Mountains to unveil: their vertical structure; factors affecting their severity; climatology of their characteristics; and their impact on surface heat flux and turbulence. It also uses a ground-based coherent Doppler wind lidar (CDWL) to observe the nighttime downslope wind events, their effects on turbulence, and their interaction with synoptic conditions. The impacts of these nighttime downslope wind events on boundary layer dynamics and dust emissions are explored at Minfeng using the vertical profiles of a ground-based CDWL along with the temporal distribution of MERRA-2 dust emissions.

2. Materials and Methods

This study relied primarily on ERA5 reanalysis data to investigate the nighttime downslope flows over the northern slope of the Kunlun Mountains and how they affect the atmosphere of Minfeng. ERA5, produced by the European Centre for Medium-Range Weather Forecasts (ECMWF), is the fifth-generation reanalysis of the global climate and weather with a spatial resolution of 0.25° × 0.25° and a temporal resolution of 1 h [32]. ERA5 is commonly used to study the regional wind field, and Huang et al. [33] demonstrated its outstanding performance in the Taklimakan desert. The "ERA5 hourly data on single levels from 1940 to present" dataset was used to access the 10 m horizontal wind components required to calculate the speed (m s^{-1}) and direction (°) of the wind, mean sea level pressure (hPa), 2 m temperature (K), and surface sensible heat flux (SSHF, W m^{-2}). The "ERA5 hourly data on pressure levels from 1940 to present" dataset was used to access the wind components (m s^{-1}), vertical velocity (Pa s^{-1}), temperature (K), and specific humidity (g kg^{-1}). The ERA5 meteorological data was obtained from the Copernicus climate data store website "https://cds.climate.copernicus.eu/ (accessed on 10 May 2024)".

Firstly, the mean sea level pressure and 10 m horizontal wind throughout China during the night of 2022 were used to analyze the nighttime synoptic conditions and the wind patterns that affect Minfeng. Nighttime refers to the period from 22:00 to 07:00 local time. After that, the nighttime downslope wind events were identified based on three locations: at Minfeng, over the slope, and above the mountain. First, Minfeng must experience southerly winds that are roughly perpendicular to the mountain range axis (between 135 and 225°), for at least 5 continuous hours without gaps during the night. Second, each selected event must have continuous downward vertical velocity over the slope. Third, the average of the surface winds above the mountaintop level for the whole duration of each selected event must be southerly (between 135 and 225°). Figure 2 shows the nighttime downslope wind events detection area, including the locations and elevations of the Minfeng, slope, and mountaintop dataset grid points. Data from these grid points were used to compute the parameters of the detection criteria. Based on these criteria, a total of 125 downslope wind events were identified. Further details of the identification procedure and supporting figures (Figure A1) are provided in Appendix A.

The vertical structure of nighttime downslope flow was investigated using a longitudinal cross-section passing through Minfeng showing the vertical velocity and the longitudinal component of the horizontal wind in two scenarios: (1) using all nighttime data, which represents the downslope flow's initial weakness and gradual intensification; and (2) using only selected downslope wind events data, which represents the hours of the intensified downslope flow. ERA5 data at multiple pressure levels were obtained for all nighttime hours in 2022 as well as for all hours corresponding to the selected events. Based on the downward vertical velocities over the slope, the selected nighttime downslope wind events were classified into three categories: weak (<0.4 Pa s^{-1}), moderate (0.4 to 0.8 Pa s^{-1}), and strong (>0.8 Pa s^{-1}). The frequency of these categorized events was calculated and analyzed for different levels of the: (1) onset time relative to sunset, considering the onset time as the moment when the direction of vertical velocity over the slope begins to change from upward to downward; (2) temperature gradient between the mountaintop and the desert surface; (3) static stability (K km^{-1}) over the peak and slope of the mountain at the moment of onset, calculated as the potential temperature gradient with respect to the height; and (4) specific humidity over the peak and slope of the mountain. This study also examined the climatology of selected nighttime downslope wind event characteristics, such as temperature and pressure gradients, downward vertical velocities over the slope, and surface wind speeds and thermal stratifications (K) at Minfeng. In addition, the impacts of nighttime downslope flow on surface heat flux and turbulence were analyzed using scattering plots between vertical velocity over the slope and SSHF at Minfeng, as well as between wind speed and turbulent kinetic energy (TKE) (m^2 s^{-2}) over the surface at Minfeng for various downslope flow intensities. The ECMWF convention for vertical fluxes is positive downwards. TKE indicates the energy associated with turbulent air motion and is commonly calculated using the variance of wind speed components [34].

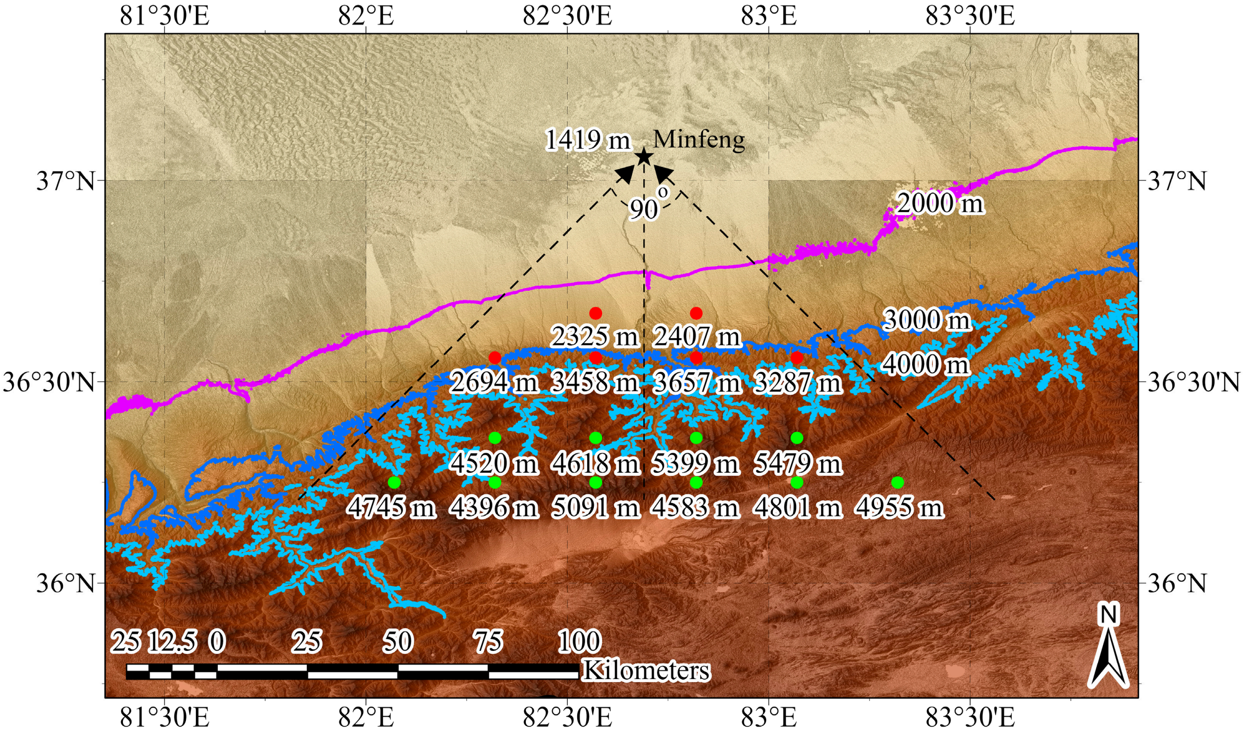

Figure 2. The nighttime downslope wind events detection area, including the locations and elevations of the Minfeng (black), slope (red), and mountaintop (green) dataset grid points; the coloured lines indicate the 2, 3, and 4 km contour lines.

A downslope wind event that occurred at night on 17 March 2022, was analyzed using the vertical profiles of a ground-based CDWL in Minfeng (82.691°E, 37.068°N). Using carrier-to-noise ratio (CNR, dB), horizontal wind speed (m s^{-1}), wind direction (°), and vertical speed (m s^{-1}), the movement of downslope winds was thoroughly recorded, starting from its initial weakness to its intensification and reaching the surface. The field experiment was conducted from July 2021 to May 2023. This lidar uses Doppler frequency shifts to detect wind along the line of sight. The velocity azimuth display scanning approach keeps a constant elevation angle of 70° while the laser beam scans several points at different yaw angles from 0° to 360° with an angle of approximately 12° between each pair and a scanning cycle of 1 min. The maximum theoretical range is 13 km, and the detection height is dynamically determined by the atmospheric aerosol distribution, typically exceeding 6 km for cloud observations. It has a 200-bin range, with resolutions of 30 m for the first 100 bins, 60 m for the second 50 bins, and 150 m for the third 50 bins [35,36]. The instrument was installed at the Minfeng County Meteorological Bureau, located within the county seat (urban setting, county radius ≈ 3 km). This study used a threshold CNR of −18 dB to exclude less accurate data. A horizontal wind direction of 0° shows wind flowing towards the north, which increases clockwise. Positive vertical wind speed implies a downward direction. For this downslope wind event, the spatial distribution of the mean sea level pressure, 10 m horizontal wind, and downward vertical velocity at 650 hPa were studied two times: after the onset of the downslope flow and after it intensified and reached the surface. The significant influence of the opposing synoptic winds on the downslope wind pattern was revealed by investigating the vertical profiles of Minfeng's CDWL under various synoptic conditions: (a) persistent strong synoptic conditions overnight on 28 March 2022, (b) persistent weak synoptic conditions overnight on 14 August 2022, and (c) strong synoptic conditions early at night on 21 April 2022.

The impacts of Taklimakan desert wind patterns on boundary layer dynamics and dust emissions were investigated during 12–18 May 2022, using the vertical profiles of Minfeng's CDWL obtained with the same scanning approach mentioned earlier, along with the temporal distribution of MERRA-2 dust emissions (kg m^{-2} s^{-1}). The Modern-Era Retrospective analysis for Research and Applications version 2 (MERRA-2) is the most current satellite-era global atmospheric reanalysis from NASA's Global Modelling and Assimilation Office (GMAO), covering the period 1980–the present at a 0.5° × 0.625° spatial resolution. The dust emissions dataset includes five size bins—bin001, bin002, bin003, bin004, and bin005—which correspond to dust particles with radius of 0.1–1, 1–1.8, 1.8–3, 3–6, and 6–10 µm, respectively [37]. Total dust emissions were calculated as the sum of emissions from all five size bins. The MERRA-2 dust emissions utilized in this study were obtained from the GES DISC website "https://disc.gsfc.nasa.gov/ (accessed on 8 August 2025)".

3. Results and Discussion

3.1. Nighttime Synoptic Conditions

The nighttime synoptic conditions were examined to illustrate the wind patterns that impact Minfeng. The mean sea level pressure (hPa) and 10 m horizontal wind (m s^{-1}) across the Taklimakan desert during the night in 2022 are shown in Figure 3. Minfeng is influenced by a northeasterly synoptic wind pattern, which is caused by the steep pressure gradient between the high-pressure system in the north (~1023 hPa) and the Taklimakan desert trough (~1014 hPa). The high-pressure system, which affects wide areas in southern Russia, eastern Kazakhstan, Mongolia, Inner Mongolia, and northern Xinjiang, develops intense winds that penetrate the Taklimakan desert through the eastern gap between its mountains.

High pressure also appears above the Taklimakan desert mountains (~1025 hPa), causing the trough to serve as a wind convergence zone, with winds arriving from all directions. During the night, the land cools radiatively through the emission of longwave radiation into the sky. Because the highlands and mountain slopes cool faster than the desert surface, the air above the mountain becomes denser and, as a result, higher in pressure compared to that over the desert surface. This localized thermal pressure gradient, in addition to the influence of gravity, generates a force that causes the denser and higher-pressure air to flow downslopes, affecting Minfeng with a southerly wind pattern. The low-pressure area in the middle of the Tibetan plateau gathers wind from the high-pressure area over its southern side. In addition, there is no large-scale wind that may be directed towards the Tibetan plateau's southern slope, resulting in synoptical downslope flow over its northern slope, implying that the nighttime downslope wind events detected at Minfeng are thermally driven as a result of the temperature and pressure differences between the mountaintop and the desert surface. To conclude, Minfeng experiences two wind patterns at night: (1) northeasterly winds from the synoptic pressure gradient, and (2) southerly winds from the thermal downslope flow.

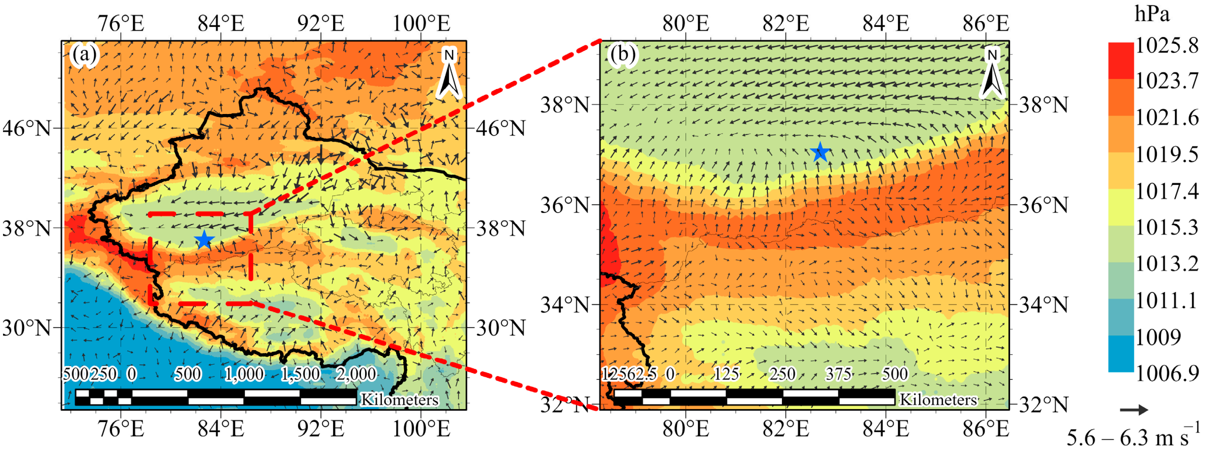

Figure 3. The mean sea level pressure (hPa, shading) overlapped by 10 m horizontal wind (m s^{-1}, vectors) across the Taklimakan desert during the night in 2022 with (**a**) 1° wind field resolution and (**b**) 0.25° wind field resolution; the blue star indicates Minfeng.

3.2. Characterization of Downslope Flow

Figure 4 shows a longitudinal cross-section passing through Minfeng and illustrating the vertical structure of the nighttime downslope flow by using the vertical velocity (Pa s^{-1}) and the longitudinal component of the horizontal wind (m s^{-1}) from both all nighttime data and selected downslope wind events data.

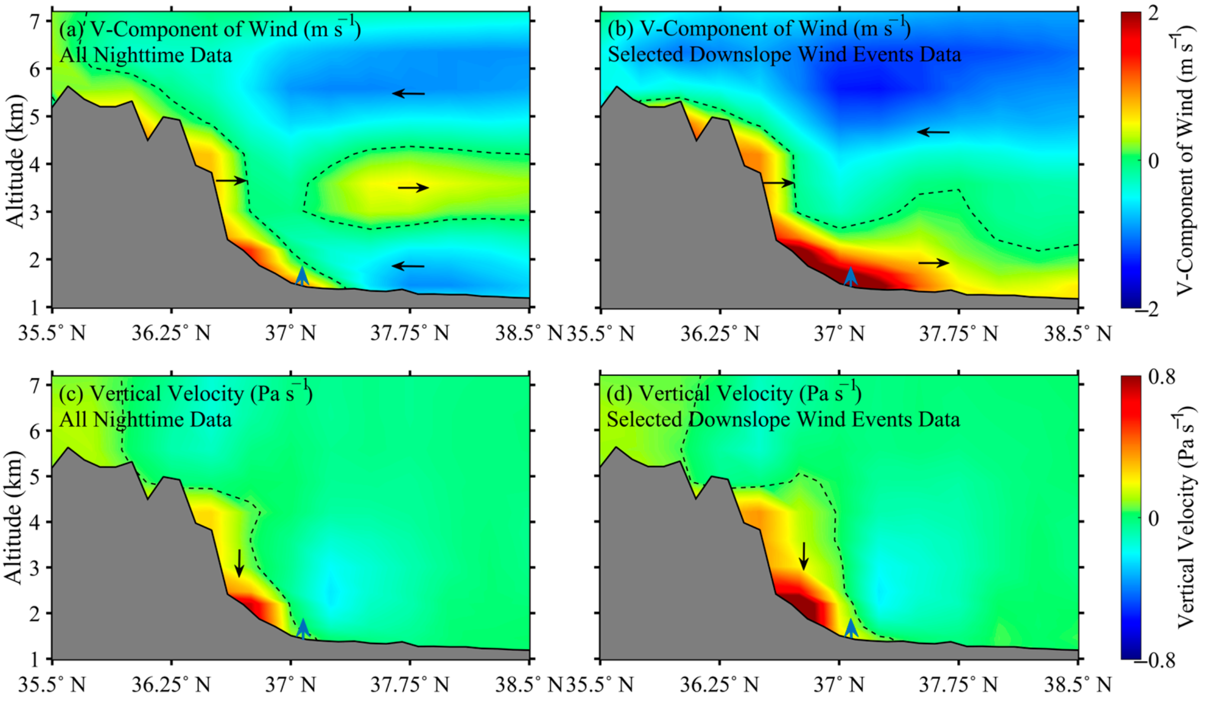

Figure 4. A longitudinal cross-section passing through Minfeng and illustrating the vertical structure of the nighttime downslope flow by using the longitudinal component of the horizontal wind (m s^{-1}, + northward, − southward) from (**a**) all nighttime data and (**b**) selected downslope wind events data, as well as the vertical velocity (Pa s^{-1}, + downward, − upward) from (**c**) all nighttime data and (**d**) selected downslope wind events data; the zero contour lines are indicated by the dashed lines; Minfeng location is indicated by the blue arrow.

During the night, the cold dense air over the mountain flows downhill and faces the opposite northeasterly synoptic winds that enter the Taklimakan desert through its eastern opening (Figure 4a–c). A portion of the downslope flow is deflected horizontally as it encounters the opposing surface wind layer, allowing the southerly winds to ride over the northeasterly winds. This phenomenon can be attributed to the idea that the thermally driven downslope flow for the majority of the night is weaker than the opposing surface synoptic wind. Also, the significant stable layer or temperature inversion over the desert surface serves as a barrier separating the downslope flow over the opposing synoptic wind. When a substantial temperature inversion forms above the surface, downslope flows often descend into the elevated part of this inversion at the height where the flow's buoyancy matches that of the desert's stratified air [38]. The horizontal extent and depth of this riding depend on factors such as the strength of the temperature inversion, the severity of the opposing synoptic wind, and the gradual intensification of the downslope flow. When the opposing synoptic winds get stronger, directional shear, along with the associated turbulence, can significantly affect the downslope flows [39,40].

While the downhill flow is initially weak, it gets more intense with time. The continuing radiative cooling, as the night progresses, increases the temperature gradient between the mountain slope and the desert surface, strengthening the downslope flow. Also, as the night progresses, cooler air from mountain slopes continues to drain down, supplying denser air to feed downslope flows. Furthermore, the air warms and is compressed adiabatically as it moves downslope. The continuous downslope flow during the night contributes to further warming of the descending air, which enhances the pressure gradient between the warmer air at lower elevations and the cooler air at higher elevations and induces the downslope flow. Park et al. [41] demonstrated that the increased pressure gradient force due to adiabatic warming along the slope amplifies downslope flow and accelerates surface winds. Moreover, Turner et al. [42] showed that strong downslope winds and adiabatic compression lead to high-temperature events and warm pools. The vertical structure of the nighttime downslope flow was further investigated using the selected downslope wind events data, which represents the hours of the intensified downslope flow (Figure 4b–d). Induced downward vertical velocities of 1.20 Pa s^{-1} are observed over the slope. In addition, the intensified downslope flow reaches the surface and spreads horizontally, with a maximum mean speed of 3.1 m s^{-1}, overcoming the opposing synoptic winds. To conclude, the initial weak downslope winds are deflected and flow horizontally over the opposing surface synoptic wind layer, but once they get intensified, they overcome these opposing winds and reach the surface.

3.3. Factors Influencing the Severity of Downslope Wind Events

The selected nighttime downslope wind events were classified into three categories depending on their downward vertical velocities over the slope: weak, moderate, and strong. Figure 5 shows the frequency of downslope wind events in the three intensity categories for different levels of the onset time relative to sunset (h), temperature gradient (K), static stability (K km^{-1}), and specific humidity (g kg^{-1}). The onset time of downslope wind events was calculated as the moment when the direction of vertical velocity over the slope begins to change from upward to downward around sunset. An hour before sunset to two hours after sunset was when most downslope wind events take place (Figure 5a). Furthermore, strong events occurred at or before sunset, while weak events occurred afterward. The earlier onset means a longer period of radiative cooling, which increases the temperature gradient between the mountaintop and desert surface and leads to stronger downslope flow. The earlier onset also causes the downslope flow to have more time to develop and intensify throughout the night due to the greater accumulation of dense air descending the mountain slopes. In addition, the early onset may coincide with the atmospheric instability conditions in the early evening, which are more favourable for the formation of strong events. In the late evening, the downslope flows subside as the atmosphere becomes more stable and horizontally stratified [43,44]. This supported the findings of Arrillaga et al. [21], who found that intense downslope flows occur around 1.5 h before sunset in the Guadarrama Mountains in the central Iberian Peninsula, Spain, during the summer of 2017. The severity of downslope wind events is significantly influenced by the temperature gradient between the mountaintop and the desert surface, with strong and moderate events dominating in greater temperature gradients (Figure 5b). The higher temperature gradient between the mountaintop and the desert surface causes a greater density difference, allowing the denser, cooler air at the mountaintop to sink due to gravitational force [45]. Colder air is denser and hence exerts higher pressure, creating a steeper pressure gradient force and consequently stronger downslope wind events.

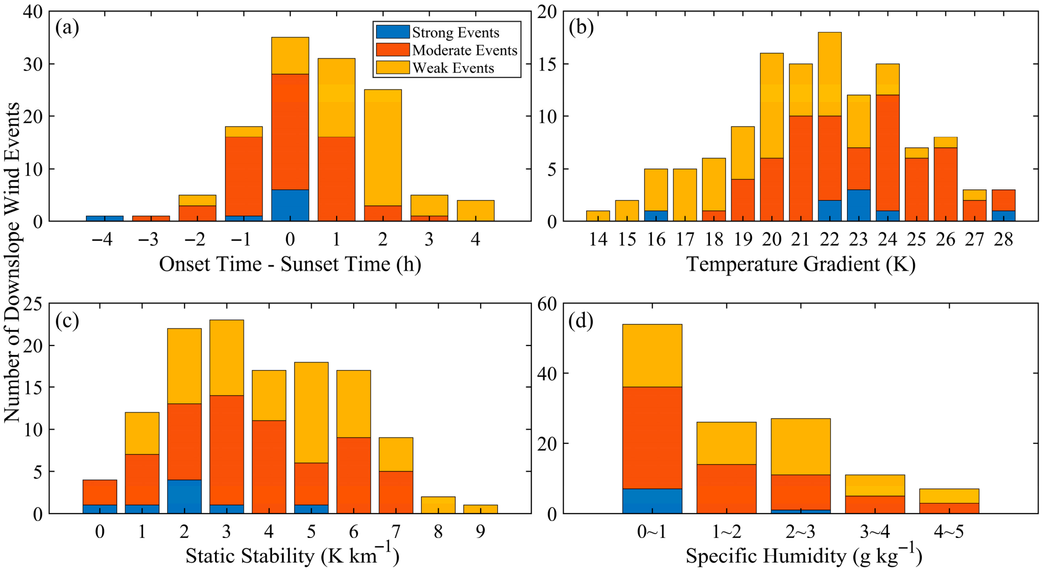

Figure 5. The frequency of downslope wind events in the three intensity categories for different levels of (**a**) the onset time relative to sunset (h), (**b**) temperature gradient (K), (**c**) static stability (K km^{-1}), and (**d**) specific humidity (g kg^{-1}).

The atmospheric static stability over the peak and slope of the mountain at the moment of onset substantially affects the severity of downslope flow, with strong events occurring in weak static stability conditions (Figure 5c). In unstable conditions, the acceleration of downslope flow caused by gravity and pressure gradients is more pronounced, leading the downslope wind events to be more severe and turbulent. On the other hand, downslope flow is weaker and less turbulent in stable conditions, which are often characterized by a strong inversion layer that inhibits the sinking motion. Strong downslope flow is less likely to form under these stable conditions because the airflow is often smoother and more laminar, travelling in layers along the slope. This inverse relationship between static stability and the intensity of downslope flow was also demonstrated by Zhong and Whiteman [46]. The specific humidity over the peak and slope of the mountain also affects the severity of downslope flow, with the highest number of events occurring in dry conditions (Figure 5d). Furthermore, in these dry conditions, strong downslope wind events occurred, which can be attributed to the enhanced radiative cooling that strengthens the temperature gradient. It is well known that under humid conditions, moisture in the air may condense and release latent heat, slowing the cooling process. Also, higher humidity levels can increase atmospheric stability and inhibit the rapid acceleration of downslope flow. Certain regions have varied humidity levels, such as the dry Colorado Plateau [47,48] or the humid Alps [49] and West Sumatra [50], which influence how intense the downslope flow is.

3.4. Climatology of Downslope Wind Events

Figure 6 depicts monthly variations in selected nighttime downslope wind events and their corresponding characteristics, including temperature (K) and pressure (hPa) gradients, downward vertical velocities over the slope (Pa s^{-1}), and surface wind speeds (m s^{-1}) and thermal stratifications (K) at Minfeng. The temperature gradient between the mountaintop and the desert surface is impacted by radiative cooling. Mountaintop cools faster than the desert surface due to increased radiative heat loss, which results in a greater temperature gradient. The monthly distribution of the pressure gradients is highly correlated with that of the temperature gradients, with a correlation coefficient of 0.79. Pressure gradients are largely caused by temperature variations; when air cools across mountain slopes, it gets denser and sinks, resulting in higher pressure at higher elevations compared to lower elevations. The highest pressure gradients detected in warmer months (from March to September) can be attributed to stronger radiative cooling at higher elevations during clear and calm nights. On the other hand, the lowest pressure gradients detected in colder months (from December to February) can be attributed to increased cloud cover, reduced radiative cooling, and stronger atmospheric stability. Bailey et al. [51] attributed the weak downslope flow to insufficient radiative cooling in the presence of clouds during their experiment in the Saguache Mountain Valley, Colorado, USA, on 19 July 2018. The nighttime downslope wind events caused by these pressure gradients and the gravitational force have a significant impact on the surface wind speeds at Minfeng. While the highest impact was observed in June, with a mean wind speed of 4.16 m s^{-1}, the lowest impact was observed in December and January, with mean wind speeds of 2.02 and 2.11 m s^{-1}, respectively.

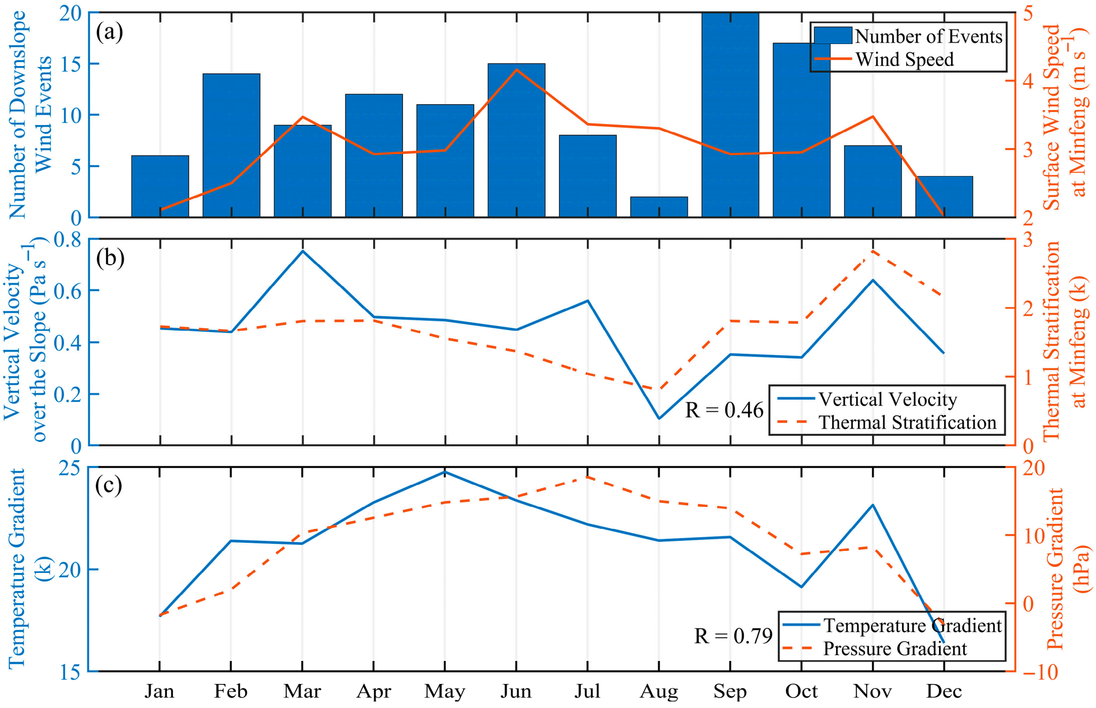

Figure 6. The monthly variations in (**a**) selected nighttime downslope wind events and surface wind speeds at Minfeng (m s^{-1}), (**b**) downward vertical velocities over the slope (Pa s^{-1}) and surface thermal stratifications at Minfeng (K), and (**c**) temperature (K) and pressure (hPa) gradients.

The weak downward vertical velocities over the slope seen in August, September, and October can be attributed to the later onset of the downslope flow in these months, with all detected events beginning at or after sunset (Table A1). This was consistent with the findings of Nadeau et al. [52], who observed a later onset of 1.5 h after sunset in their summer field campaign in the Swiss Alps from July to September 2010 to monitor the evening transition of slope flows. Moreover, August showed the lowest number of nighttime downslope wind events, with only two detected, which can be associated with the influence of opposing synoptic winds that peak in August. The opposing synoptic winds at the desert surface can cause upward flow over the slope, potentially countering the downward flow of downslope winds. The highest temperatures in August can reduce the density of surface air, allowing it to be easily pushed upslope by opposing synoptic winds. In addition, the impact of the opposing synoptic winds on the downward vertical velocity over the slope can be controlled by the surface thermal stratification at the desert level. The surface thermal stratification at Minfeng and the downward vertical velocity over the slope showed a moderate correlation of 0.46. When the thermal stratification at the desert level is strong, it can effectively reduce the upward motion caused by the opposing synoptic winds, allowing more pronounced downward vertical velocities over the slope. In contrast, when the thermal stratification is weak, the upward motion caused by the opposing synoptic winds can disrupt the downslope flow, resulting in weaker downward vertical velocities over the slope. August, with the lowest surface thermal stratification of 0.81 K, had the lowest downward vertical velocity over the slope of 0.10 Pa s^{-1}, which consequently reduces the frequency of downslope wind events in this month.

3.5. Turbulence Caused by Downslope Wind Events

Figure 7 depicts scattering plots of the relationships between vertical velocity over the slope (Pa s^{-1}) and surface sensible heat flux (SSHF) at Minfeng (W m^{-2}), as well as wind speed (m s^{-1}) and turbulent kinetic energy (TKE) (m^2 s^{-2}) over the surface at Minfeng, for various downslope flow intensities. The SSHF increases as the downward vertical velocity over the slope increases, with mean values of 9.38, 11.76, and 19.33 W m^{-2} for weak (0.27 Pa s^{-1}), moderate (0.57 Pa s^{-1}), and strong (0.92 Pa s^{-1}) downslope flow, respectively, suggesting that nighttime downslope flow enhances the amount of transferred heat at the surface. As air moves downslope, it undergoes adiabatic compression, resulting in a rise in its temperature. When the warmer air reaches the relatively cooler desert surface, the transfer of heat between the surface and the atmosphere is enhanced, and the SSHF is increased [53,54]. Also, the surface wind caused by the downslope flow can increase turbulent mixing, which consequently amplifies the SSHF.

The mean wind speed and TKE over the surface at Minfeng caused by the downslope wind events are 2.76 m s^{-1} and 3.48 m^2 s^{-2} for weak downslope flow, 3.25 m s^{-1} and 3.91 m^2 s^{-2} for moderate downslope flow, and 3.85 m s^{-1} and 4.63 m^2 s^{-2} for strong downslope flow. Mechanical turbulence can be formed when the downslope flow hits the desert surface with high surface winds. In addition, the mixing of the warmer, downslope air with the cooler surface air can generate thermal turbulence through convective processes when the warmer air rises and the cooler air above sinks. The reach of the warmer air to the cooler surface weakens the temperature inversion and disrupts the stable stratification of the lower atmosphere, allowing for induced mixing and turbulence. Evan [55] and Pokharel et al. [56] showed the significant role of downslope winds in generating dust storms by causing considerable surface wind shear and turbulence. Carvalho et al. [57] illustrated how downslope flow-induced high winds and gusts contribute to critical fire weather and aviation hazards.

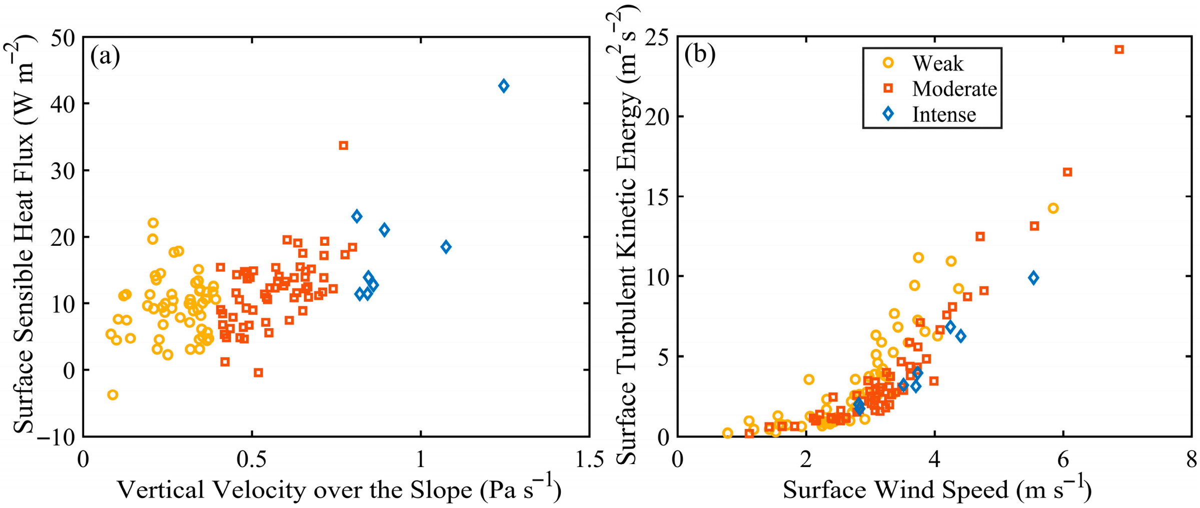

Figure 7. Scattering plots of the relationships between (**a**) vertical velocity over the slope (Pa s^{-1}) and surface sensible heat flux at Minfeng (W m^{-2}), as well as (**b**) wind speed (m s^{-1}) and turbulent kinetic energy over the surface at Minfeng (m^2 s^{-2}), for various downslope flow intensities.

3.6. Lidar-Based Detection of Downslope Flow

The vertical profiles of a CDWL can also be used to identify the vertical structure of nighttime downslope flow and its impact on turbulence. A downslope wind event that occurred at night on 17 March 2022, was investigated in this section. Figure 8 shows the vertical profiles of CDWL in Minfeng between 19:00 on 17 March and 12:00 on 18 March 2022, including CNR (dB), horizontal wind speed (m s^{-1}), wind direction (°), and vertical speed (m s^{-1}).

Between 19:00 and 22:00, northern and northeastern winds were observed over the surface to an altitude of 2 km, representing the synoptic winds that enter the Taklimakan desert from its eastern open. In addition, southern and southeastern winds were observed above the opposing synoptic wind layer, covering the height above 2 km altitude, representing the winds coming from the downslope flow. This demonstrates the weakness of the downslope flow after its onset, allowing it to be easily deflected horizontally when it encounters the opposing synoptic wind layer. A gradual sinking of the southerly wind layer was seen after 22:00, implying the intensification of the downslope flow with time due to (1) the continuous radiative cooling, which increases the temperature gradient between the mountain slope and the desert surface; (2) the continuous drainage of cooler air from mountain slopes to feed downslope flows; and (3) the adiabatic compression and warming of the descending air, which enhances the pressure gradient between the cooler air at higher elevations and the warmer air at lower elevations. The northerly synoptic wind layer over the surface showed higher wind speeds of around 12 m s^{-1} starting from 22:00 until its disappearance at 2:00 when the downslope flow became more intense and reached the surface. The wind shear generated by the shift in wind direction between the northerly and southerly wind layers causes turbulence, particularly between 22:00 and 00:00, when the surface synoptic winds are at their highest speed. After reaching the surface and overcoming the opposing synoptic winds, the downslope flow began to spread horizontally, increasing in speed and height over time. Mechanical turbulence was generated over the surface at 4:00 when the downslope flow hit the desert surface at a high speed of roughly 15 m s^{-1}. The southerly winds caused by the downslope flow persisted at this high speed until 8:00 and continued to affect the surface until around 11:30 when they began to disappear.

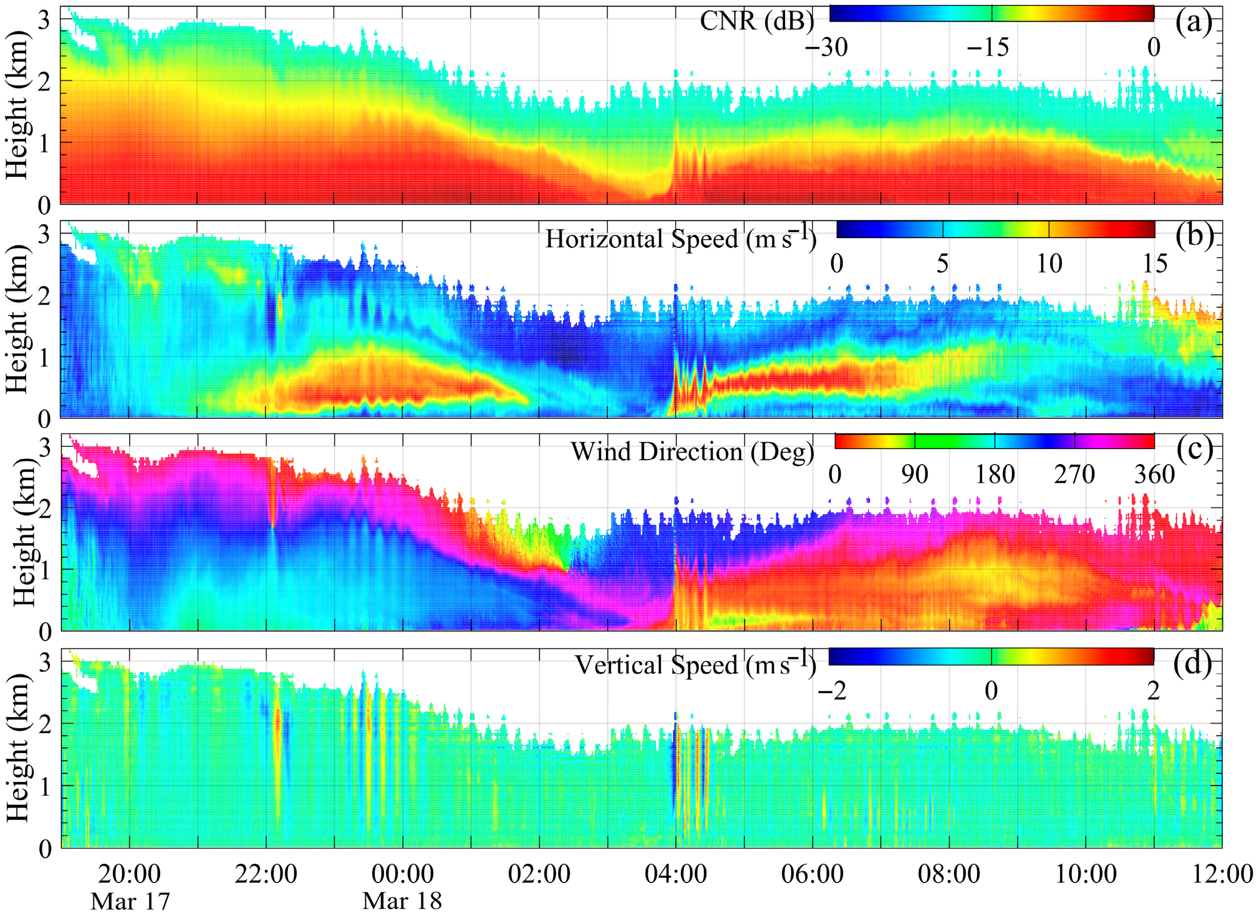

Figure 8. The vertical profiles of CDWL in Minfeng between 19:00 on 17 March and 12:00 on 18 March 2022: (**a**) CNR (dB); (**b**) horizontal wind speed (m s^{-1}); (**c**) wind direction (°); and (**d**) vertical speed (m s^{-1}).

The pressure and wind conditions at the onset of the downslope flow, when it was weak, were compared to those when it strengthened and reached the surface. Figure 9 shows the spatial distribution of the mean sea level pressure (hPa), 10 m horizontal wind (m s^{-1}), and downward vertical velocity at 650 hPa (Pa s^{-1}) at two times: after the onset of the downslope flow at 21:00 on 17 March and after the reach of the downslope flow to the surface at 3:00 on 18 March.

At the onset (Figure 9a–c), the pressure gradient between the mountaintop and the desert surface at Minfeng was about 16 hPa, causing the downslope flow to be weak and the opposing synoptic winds to prevail over the surface. Northeastern synoptic winds hit Minfeng with a speed of around 3 m s^{-1}. The increased height between the mountaintop and the desert surface near 81°E, which increases the pressure gradient, led to a relatively higher impact of the downslope flow in this region. However, due to the weakness of the downslope flow after its onset and its deflection above the opposing synoptic winds, downward vertical velocities of around 0.5 Pa s^{-1} were seen quite far from the slope. As the night progresses, the pressure gradient between the mountaintop and the desert surface at Minfeng increases. It was around 24 hPa when the downslope flow reached the surface and hit Minfeng with southeasterly winds at a speed of roughly 6 m s^{-1} (Figure 9b–d). As the downslope flow intensified and overcame the opposing synoptic winds, strong downward vertical velocities of around 1.3 Pa s^{-1} prevailed across the slope.

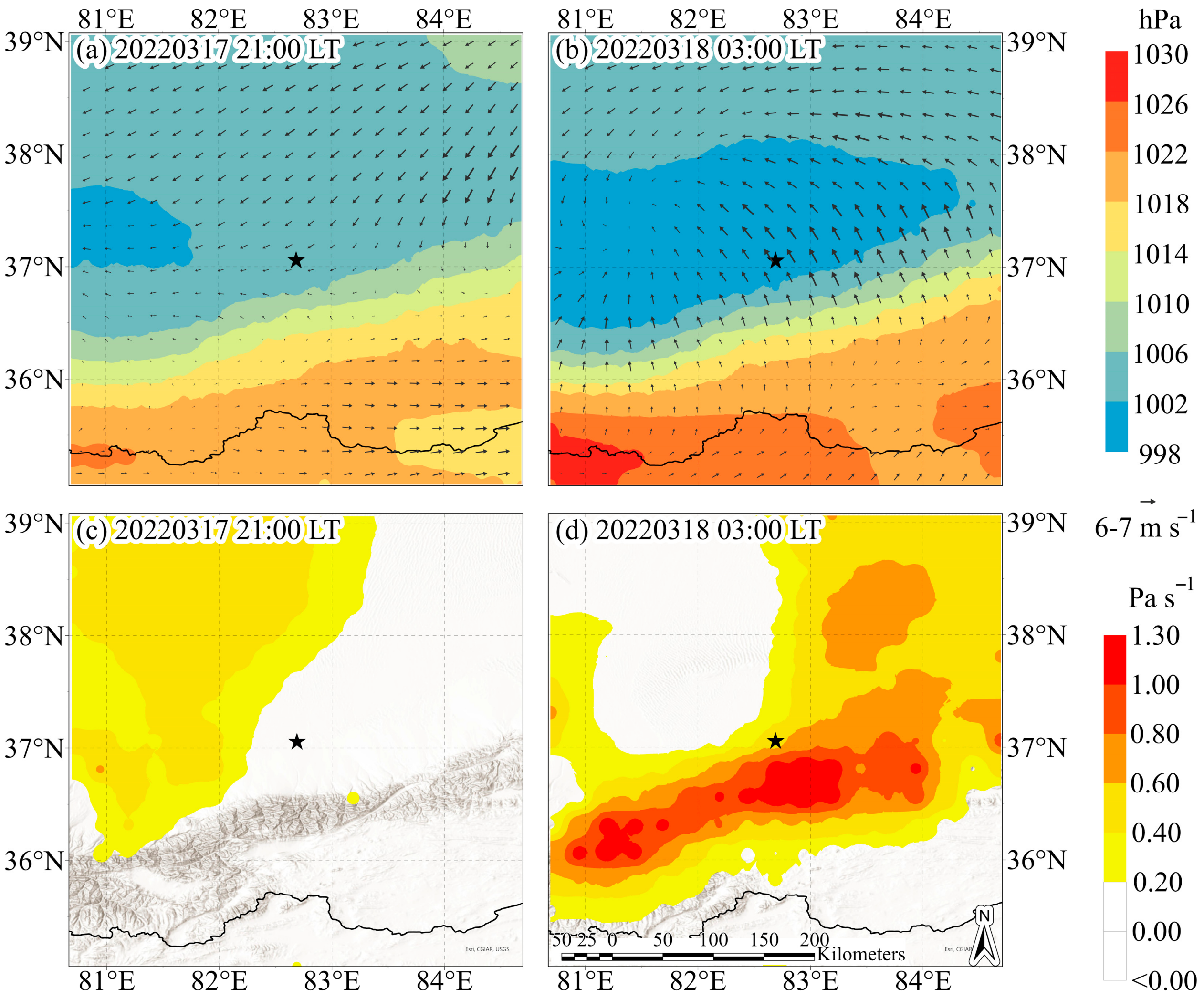

Figure 9. The spatial distribution of (**a**,**b**) the mean sea level pressure (hPa, shading) overlapped by 10 m horizontal wind (m s^{-1}, vectors), and (**c**,**d**) the downward vertical velocity at 650 hPa (Pa s^{-1}, shading) after the onset of the downslope flow at 21:00 on 17 March and after the reach of the downslope flow to the surface at 3:00 on 18 March; the black star indicates Minfeng.

3.7. Interaction Between Downslope and Synoptic Wind Patterns

Investigating the vertical profiles of Minfeng's CDWL under various synoptic conditions reveals the significant influence of the opposing synoptic winds on the downslope wind pattern. Figure 10 shows the vertical profiles of CDWL in Minfeng, including CNR (dB), horizontal wind speed (m s^{-1}), wind direction (°), and vertical speed (m s^{-1}), during (a) persistent strong synoptic conditions overnight on 28 March 2022, (b) persistent weak synoptic conditions overnight on 14 August 2022, and (c) strong synoptic conditions early at night on 21 April 2022.

On 28 March 2022, a strong synoptic wind event hit the Taklimakan desert with a peak speed of 16 m s^{-1} and persisted throughout the night, preventing the downslope flow from reaching the surface. The downslope flow was deflected above the opposing synoptic wind layer at an altitude of 4 km from its onset until around 3:30. Although the continuous radiative cooling and drainage of cooler air as the night progresses, continuous intense synoptic winds can alter the typical pattern of nighttime downslope flow by preventing it from sinking. On 14 August 2022, weak synoptic conditions prevailed in the Taklimakan desert throughout the night, allowing the nighttime downslope winds to flow smoothly and without deflection. The downslope flow reached the surface early, around 22:30, accompanied by significant mechanical turbulence. The southerly downslope winds spread over the surface, covering a height of 2 km and reaching their peak speed of 13 m s^{-1} at 06:00. On 21 April 2022, strong synoptic winds with a speed of 14 m s^{-1} were seen early at night within a height of 3 km, delaying the appearance of nighttime downslope flow. As the synoptic winds weakened at around 00:30, the downslope winds began to sink and increase in speed gradually. When the downslope winds peaked at 07:00, they appeared at the surface and prevailed through 3 km. Based on these three case studies, it is demonstrated that opposing synoptic winds have a major impact on the downslope wind pattern.

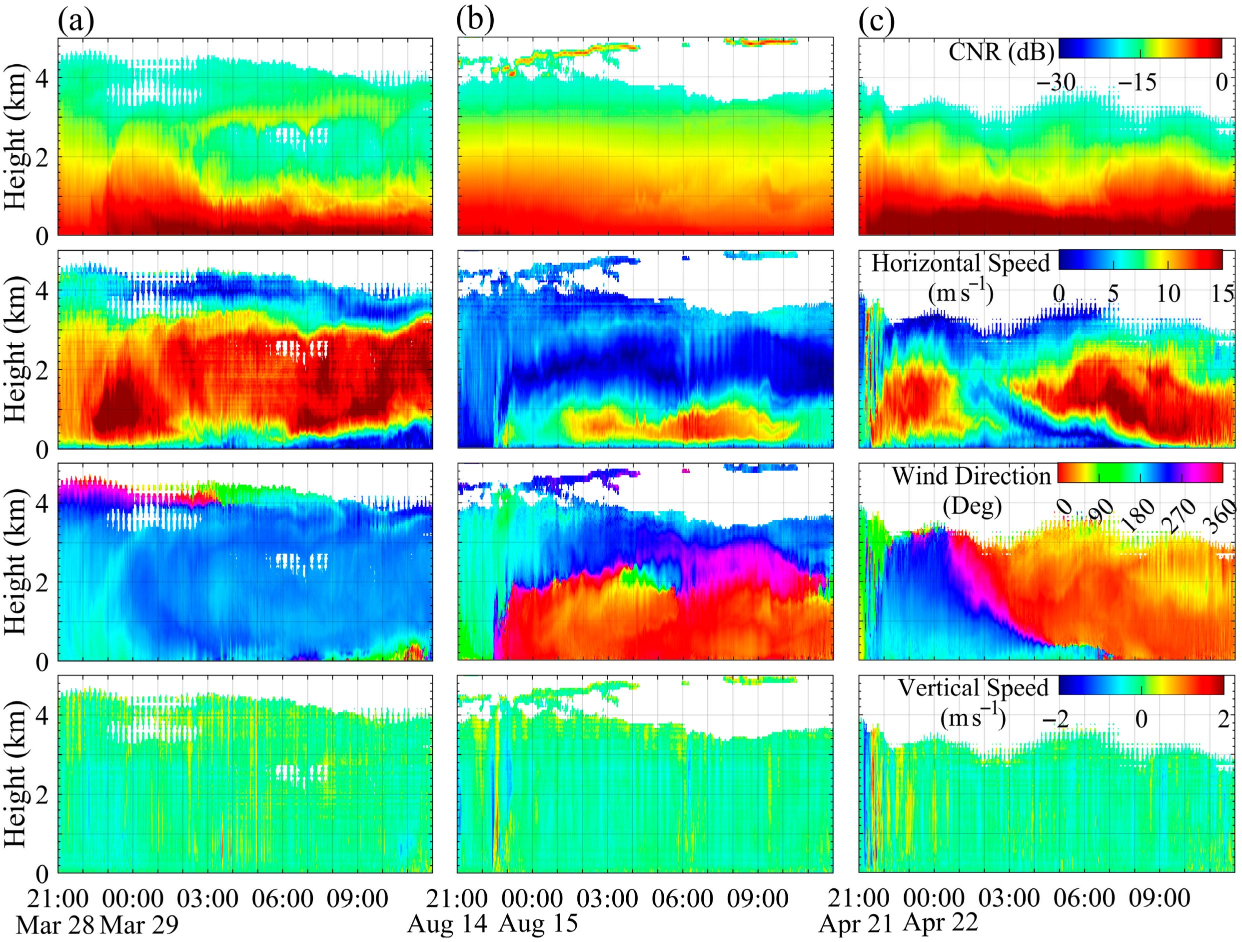

Figure 10. The vertical profiles of CDWL in Minfeng, including CNR (dB), horizontal wind speed (m s^{-1}), wind direction (°), and vertical speed (m s^{-1}), during (**a**) persistent strong synoptic conditions overnight on 28 March 2022, (**b**) persistent weak synoptic conditions overnight on 14 August 2022, and (**c**) strong synoptic conditions early at night on 21 April 2022.

3.8. Impact of Downslope Winds on Dust Emissions

The vertical profiles of Minfeng's CDWL can be used to investigate the impact of nighttime downslope wind events on boundary layer dynamics and dust emissions. Figure 11 shows the vertical profiles of CDWL in Minfeng during 12–18 May 2022, including CNR (dB), vertical speed (m s^{-1}), horizontal wind speed (m s^{-1}), and wind direction (°), along with the temporal distribution of MERRA-2 dust emissions (kg m^{-2} s^{-1}).

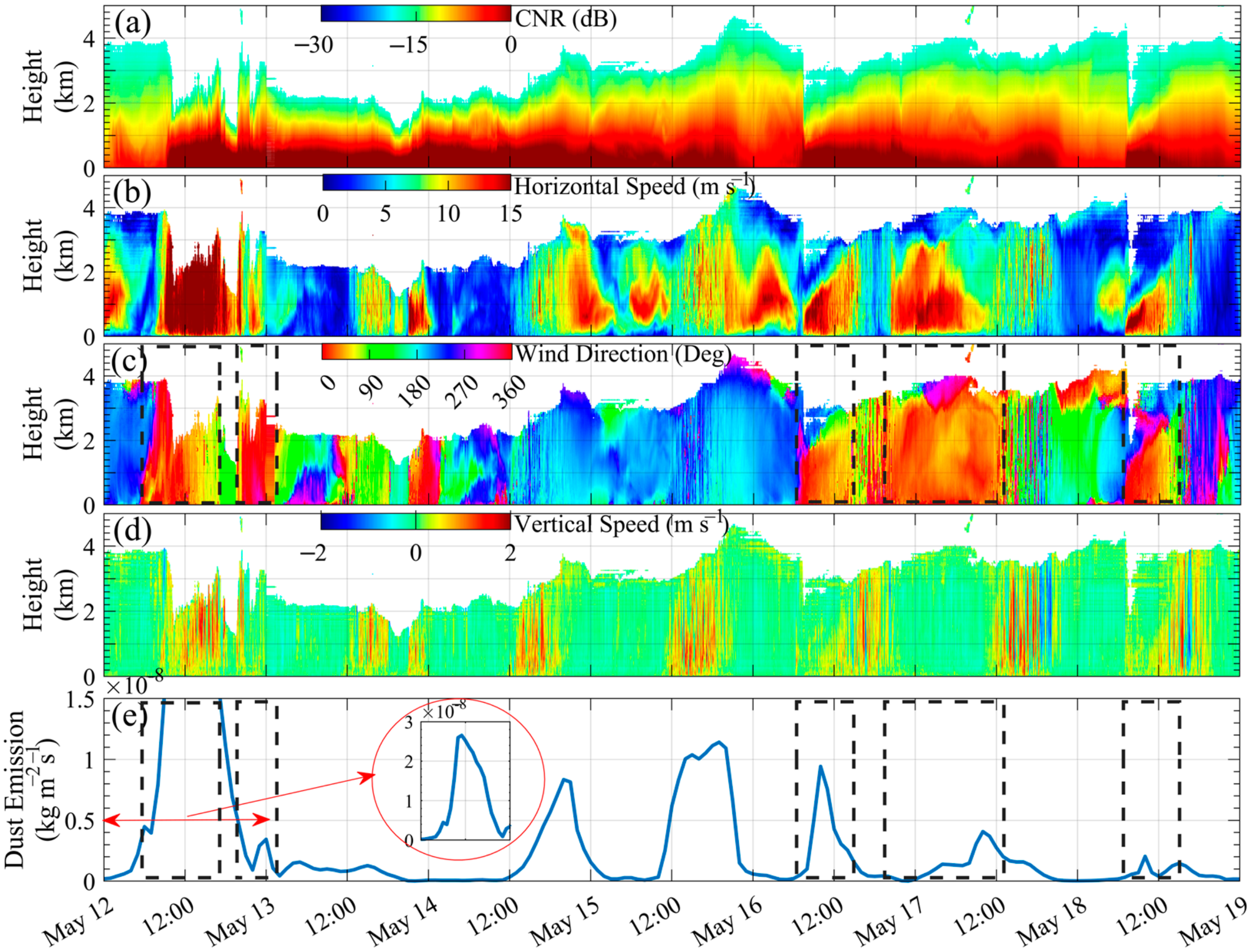

Figure 11. The vertical profiles of CDWL in Minfeng during 12–18 May 2022: (**a**) CNR (dB); (**b**) horizontal wind speed (m s^{-1}); (**c**) wind direction (°); and (**d**) vertical speed (m s^{-1}), along with (**e**) the temporal distribution of MERRA-2 dust emissions (kg m^{-2} s^{-1}); the dashed boxes indicate the periods between the onset and end of each downslope wind event; the peak dust emission on May 12 exceeds the vertical scale and is shown separately in the circle.

At 00:00 on 12 May, a northeastern synoptic wind with a speed of 12 m s^{-1} was observed within a height of 3 km, delaying the appearance of nighttime downslope winds. The dust emission at that time was 0.02 × 10^{-8} kg m^{-2} s^{-1}, and the lidar detection range was ~4 km. When the synoptic winds weakened, the southerly downslope winds appeared at the surface at 5:00, increasing in speed and height with time, and peaked at 9:00 with a speed of 18 m s^{-1}. This was accompanied by an increase in dust emissions to a peak of 2.65 × 10^{-8} kg m^{-2} s^{-1} at 11:00, leading to an intensified signal strength and a decrease in detection range to ~2 km. After that, while dust emissions were gradually decreasing to reach 0.09 × 10^{-8} kg m^{-2} s^{-1} at 22:00, a new southerly downslope wind event beginning at 20:00 could increase dust emissions to 0.34 × 10^{-8} kg m^{-2} s^{-1} at 00:00 on 13 May. The desert experienced southerly downslope winds of a speed of 16 m s^{-1} at 21:00 on 13 May, with low impact on dust emissions. Some northeasterly synoptic wind events of a speed of 12 m s^{-1} between 14 May, 15:00, and 16 May, 6:00 caused dust emissions to increase and record peaks of 0.83 × 10^{-8} kg m^{-2} s^{-1} at 20:00 on 14 May and 1.14 × 10^{-8} kg m^{-2} s^{-1} at 19:00 on 15 May. The detection range gradually expanded to ~4 km with low CNR values, before the appearance of southerly downslope winds of a speed of 16 m s^{-1} at 6:00 on 16 May, which increased CNR values, reduced the detection range to 3 km, and raised dust emissions to 0.94 × 10^{-8} kg m^{-2} s^{-1} at 10:00. In weak synoptic conditions, southerly downslope winds can prevail throughout the night, as happened on 17 May, in which dust emissions increased to 0.41 × 10^{-8} kg m^{-2} s^{-1} at 10:00. While, on the other hand, strong synoptic conditions can prevent downslope flow from reaching the surface, as happened on the night of 18 May, in which downslope winds rode over synoptic winds in the early night and reached the surface at 7:00 after the weakness of synoptic winds, raising dust emissions to 0.20 × 10^{-8} kg m^{-2} s^{-1} at 10:00. Considering this, synoptic and downslope wind patterns greatly influence the Taklimakan desert's air quality. It was demonstrated that dust events frequently occur in the Taklimakan desert [58], with dust can be lifted up to 5 km from the ground [59].

4. Conclusions

This study investigated nocturnal downslope wind events in the Taklimakan desert to reveal their vertical structure, influencing factors, climatology, and impacts on boundary layer dynamics and dust emissions. The nighttime synoptic conditions showed that Minfeng experiences two wind patterns at night: (1) northeasterly winds from the synoptic pressure gradient, and (2) southerly winds from the thermally downslope flow. The downslope wind events of the northern slope of the Kunlun Mountains that impact Minfeng's atmospheric boundary layer were detected. 125 nighttime downslope wind events in 2022 were detected based on three criteria: at Minfeng, over the slope, and above the mountain.

The horizontal deflection of a portion of the downslope flows when they encounter the opposing northeasterly synoptic wind layer, allowing the southerly winds to ride over the northeasterly winds, demonstrated the initial weakness of the downslope flow. As the night progresses, the downslope flow gradually strengthens due to continued radiative cooling, dense air drainage, and adiabatic warming. As the downslope flows intensify, they overcome the opposing synoptic winds and reach the surface, where they begin a horizontal spread. The opposing synoptic wind conditions completely influence the downslope flow pattern.

The majority of downslope wind events occur between an hour before to two hours after sunset, with the strongest occurring at or before sunset due to the longer period of radiative cooling and intensification, as well as the early evening atmospheric instability conditions that are more conducive to the formation of strong events. Strong and moderate events dominate at higher temperature gradients due to the larger difference in density and pressure, which accelerates downslope flow. Strong events also occur in weak static stability conditions, in which the acceleration of downslope flow is more pronounced. Stable conditions with a strong inversion layer inhibit the sinking motion, and the airflow is often smoother and more laminar, moving in layers down the hill. Furthermore, the majority of events, including the strong ones, occur during dry conditions, which can be attributed to enhanced radiative cooling that strengthens the temperature gradient. Air moisture may slow the cooling process and increase atmospheric stability, which inhibits the rapid acceleration of downslope flow.

Surface wind speeds at Minfeng increased in warmer months, particularly in June, due to higher pressure gradients caused by stronger radiative cooling during clear and calm nights, whereas they decreased in colder months, especially in December and January, due to lower pressure gradients caused by increased cloud cover, reduced radiative cooling, and stronger atmospheric stability. However, the later onset of downslope flow in August, September, and October caused weak downward vertical velocities over the slope. Moreover, August had the fewest nighttime downslope wind events, which can be attributed to the coincidence with the opposing synoptic wind peak, the highest temperatures that reduce surface air density, and the lowest surface thermal stratification, resulting in disruption of downslope flow and weakening of downward vertical velocities over the slope.

Nighttime downslope flow, which promotes heat transfer to the surface owing to adiabatic warming, as well as the resulting surface wind, which increases turbulent mixing, all contribute to an increase in surface sensible heat flux. While mechanical turbulence can be generated when downslope flow hits the desert surface, thermal turbulence can be generated when warmer, downslope air reaches the cooler surface, weakening temperature inversion and disrupting stable stratification of the lower atmosphere, allowing for induced mixing and turbulence.

The lidar could significantly capture the horizontal flow of the downslope winds above the opposing synoptic wind layer, as well as their gradual sinking and reach to the surface. The lidar also detected turbulence induced by wind shear as a result of the shift in wind direction between the northerly and southerly wind layers, as well as turbulence generated when the downslope flow hit the desert surface at high speed. The downslope flow spreads horizontally after reaching the surface, increasing in speed and height with time and affecting the surface. Downslope winds substantially increase dust emissions and deteriorate the air quality of the Taklimakan desert. During dust events, the lidar signal strength increases, and the detection range decreases.

Author Contributions: Conceptualization, H.X.; methodology, M.E. and H.X.; software, M.E., L.S. and T.W.; validation, H.X.; formal analysis, M.E. and H.X.; investigation, M.E. and L.S.; resources, M.E., L.S. and T.W.; data curation, M.E., L.S. and T.W.; writing—original draft preparation, M.E.; writing—review and editing, M.E. and H.X.; visualization, M.E.; supervision, H.X. All authors have read and agreed to the published version of the manuscript.

Funding: This research received no external funding.

Data Availability Statement: The data presented in this study are available on request from the corresponding author. The ERA5 meteorological data is freely available at the Copernicus climate data store website "https://cds.climate.copernicus.eu/ (accessed on 10 May 2024)". The MERRA-2 dust emissions can be freely accessed at the GES DISC website "https://disc.gsfc.nasa.gov/ (accessed on 8 August 2025)".

Conflicts of Interest: The authors declare no conflicts of interest.

Appendix A

Appendix A.1. Detection Criteria of Downslope Wind Events

Figure A1 shows wind roses: at Minfeng for all night hours; above the mountaintop level for all night hours; and at Minfeng for the hours of the selected events, as well as boxplots of the monthly vertical velocity distribution over the slope for all night hours. Wind direction is expressed as the direction from which the wind originates, meaning that 0° indicates a northerly wind. The wind rose at Minfeng for all night hours in 2022 (Figure A1a) reveals that the prevailing wind direction varies from 30° to 250°, illustrating the northeasterly synoptic and southerly downslope wind patterns. The most frequent winds typically originate from the south. This site commonly experiences weak to moderate winds, with rare occurrences of intense winds. The first criterion for the detection of downslope wind events is to find southerly winds (between 135 and 225°) at Minfeng lasting for at least five continuous hours without gaps. 157 downslope wind events were selected after applying the first criterion.

The rapid cooling of highlands and mountain slopes causes the air to become denser and gravitationally pulled downward. The vertical velocity over the slope was calculated as the data average of six grid points between 2 and 4 km contours, with the nearest pressure level above each grid point's elevation being used. The vertical resolution of ERA5 pressure levels is coarse; however, the objective of this study is not to resolve fine-scale vertical structures but rather to derive a representative estimate of the vertical velocity over the slope region for event detection purposes. The monthly distribution of vertical velocity over the slope for all night hours in 2022 (Figure A1d) shows that downward flow prevails in all months except August, with median vertical velocities ranging from 0.201 to 0.425 Pa s^{-1}. August shows prevailing upward flow, with a median vertical velocity of -0.013 Pa s^{-1}, due to the lower thermal stratification over the surface and higher temperatures that reduce surface air density, allowing air to easily flow upslope under the force of synoptic northeasterly winds. The upward vertical velocity outliers also indicate the significant effect of the opposite synoptic northeasterly winds. On the other hand, the most significant downward flow is observed in March, with median, 75th percentile, and maximum vertical velocity values of 0.425, 0.705, and 1.481 Pa s^{-1}, respectively. The second criterion for the detection of downslope wind events is to find continuous downward vertical velocity over the slope for all hours of the 157 selected events. After removing the hours of the upward flow, 27 events were modified, and 18 events were removed. 139 downslope wind events were selected after applying the first and second criteria. The surface wind speed above the mountaintop level was calculated as the data average of 10 grid points. The wind rose at the mountaintop level for all night hours in 2022 (Figure A1b) reveals that the prevailing wind direction varies from 150° to 180°, illustrating the northward flow of the dense high-pressure air. The lower wind speeds at the mountaintop level compared to those at Minfeng demonstrate that the nightly downhill flow over the slope under gravitational force significantly intensifies the surface wind speeds at Minfeng. The third criterion for the detection of downslope wind events is to find southerly winds above the mountaintop level (between 135 and 225°) as an average of the selected event hours. 14 events, with average winds not being southerly, were removed. 125 downslope wind events were selected after applying all three criteria. The surface wind speeds at Minfeng during the hours of the 125 selected downslope wind events are represented in the wind rose in Figure A1c.

The criteria used for identifying nocturnal downslope wind events in this study are adapted based on both the physical characteristics of nocturnal downslope flows in the Taklimakan desert and previous studies of similar downslope wind systems [21,26,27]. The combination of the three criteria (southerly surface winds at Minfeng, consistent downward vertical velocity over the slope, and southerly winds above the mountaintop) is developed to suit the unique topography and meteorological conditions of the Taklimakan desert. The threshold of at least 5 continuous nighttime hours was selected to ensure that only well-developed, sustained downslope events were included in the analysis, while excluding short-lived or transitional flows that may not reflect true downslope processes. This threshold balances the need for capturing representative events with maintaining a sufficiently large sample size for climatological analysis. The wind direction range of 135–225° was chosen to represent southerly flow roughly perpendicular to the mountain range, based on the orientation of the terrain near Minfeng. This range captures the downslope drainage from the Kunlun Mountains toward the desert basin. The requirement for consistent downward vertical velocity over the slope is based on the fundamental dynamics of downslope flows, which are driven by gravitational drainage of cooled, dense air. The inclusion of southerly flow above the mountaintop level helps confirm that the observed surface flow is not part of a broader synoptic pattern but rather a distinct local drainage event.

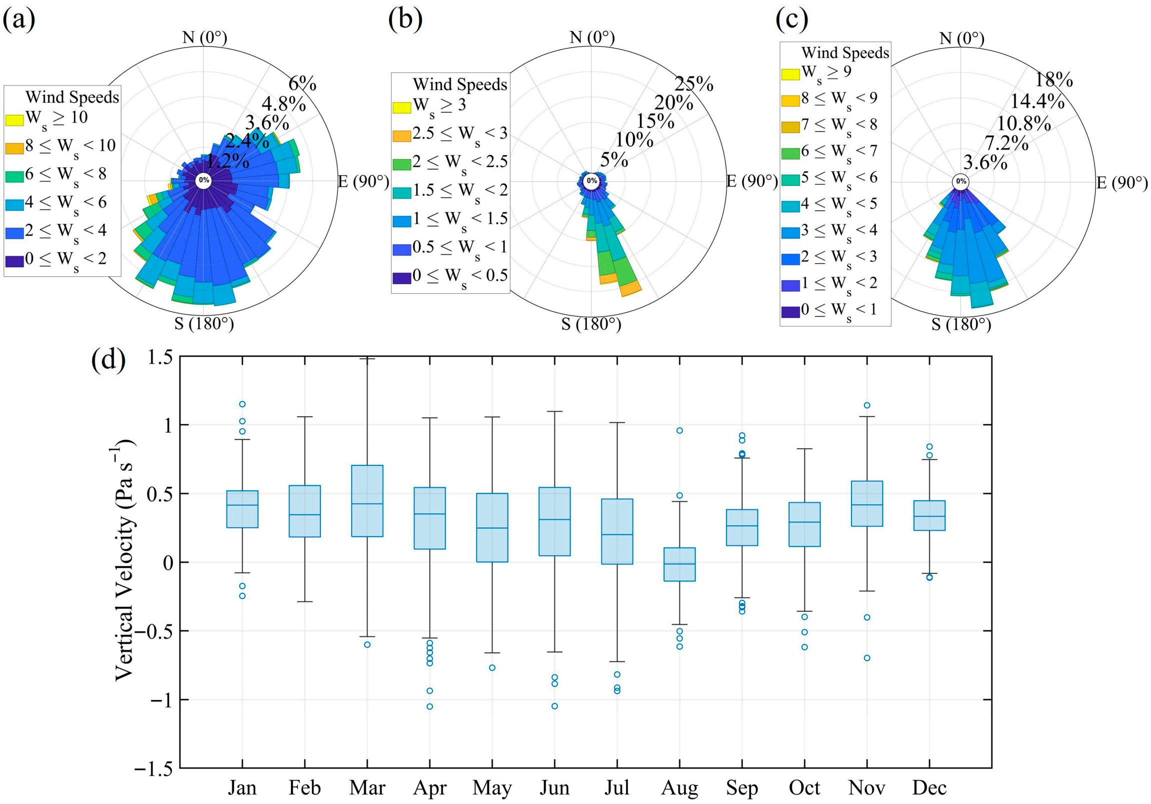

Figure A1. Wind roses: (**a**) at Minfeng for all night hours; (**b**) above the mountaintop level for all night hours; and (**c**) at Minfeng for the hours of the selected events, as well as (**d**) boxplots of the monthly vertical velocity distribution over the slope for all night hours (+ downward; − upward; each box's central, bottom, and top lines correspond to the median, 25th, and 75th percentiles, respectively; the whiskers extend to the minimum and maximum data points; while outliers are indicated as circles).

Appendix A.2. The Monthly Distribution of the Onset Time

Table A1. The monthly mean onset times relative to sunset of the downslope wind events.

Month	Jan	Feb	Mar	Apr	May	Jun	Jul	Aug	Sep	Oct	Nov	Dec
Onset-Sunset	0	1	0	1	1	0	0	2	2	1	0	1

References

1. Mehta, M.; Singh, N. Global trends of columnar and vertically distributed properties of aerosols with emphasis on dust, polluted dust and smoke-inferences from 10-year long CALIOP observations. *Remote Sens. Environ.* **2018**, *208*, 120–132. [CrossRef]
2. Chen, S.; Huang, J.; Kang, L.; Wang, H.; Ma, X.; He, Y.; Yuan, T.; Yang, B.; Huang, Z.; Zhang, G. Emission, transport, and radiative effects of mineral dust from the Taklimakan and Gobi deserts: Comparison of measurements and model results. *Atmos. Chem. Phys.* **2017**, *17*, 2401–2421. [CrossRef]
3. Hu, Z.; Huang, J.; Zhao, C.; Bi, J.; Jin, Q.; Qian, Y.; Leung, L.R.; Feng, T.; Chen, S.; Ma, J. Modeling the contributions of Northern Hemisphere dust sources to dust outflow from East Asia. *Atmos. Environ.* **2019**, *202*, 234–243. [CrossRef]
4. Xie, S.; Yu, T.; Zhang, Y.; Zeng, L.; Qi, L.; Tang, X. Characteristics of PM_{10}, SO_2, NO_x and O_3 in ambient air during the dust storm period in Beijing. *Sci. Total Environ.* **2005**, *345*, 153–164. [CrossRef]
5. Liang, C.-S.; Yu, T.-Y.; Lin, W.-Y. Source apportionment of submicron particle size distribution and $PM_{2.5}$ composition during an Asian dust storm period in two urban atmospheres. *Aerosol Air Qual. Res.* **2015**, *15*, 2609–2624. [CrossRef]
6. Zong, X.; Xia, X.; Che, H. Validation of aerosol optical depth and climatology of aerosol vertical distribution in the Taklimakan Desert. *Atmos. Pollut. Res.* **2015**, *6*, 239–244. [CrossRef]
7. Hatchett, B.J.; Kaplan, M.L.; Nauslar, N.J.; Smith, C.M.; Nelson, K. Slope Winds. In *Encyclopedia of Wildfires and Wildland-Urban Interface (WUI) Fires*; Springer: Cham, Switzerland, 2020; pp. 922–930. [CrossRef]

8. Farina, S.; Zardi, D. Understanding thermally driven slope winds: Recent advances and open questions. *Bound.-Layer Meteorol.* **2023**, *189*, 5–52. [CrossRef]
9. Whiteman, C.D. *Mountain Meteorology: Fundamentals and Applications*; Oxford University Press: Oxford, UK, 2000.
10. Poulos, G.; Zhong, S. An observational history of small-scale katabatic winds in mid-latitudes. *Geogr. Compass* **2008**, *2*, 1798–1821. [CrossRef]
11. Zardi, D.; Whiteman, C.D. Diurnal mountain wind systems. In *Mountain Weather Research And Forecasting: Recent Progress and Current Challenges*; Springer: Dordrecht, The Netherlands, 2012; pp. 35–119. [CrossRef]
12. Jensen, D.D.; Nadeau, D.F.; Hoch, S.W.; Pardyjak, E.R. The evolution and sensitivity of katabatic flow dynamics to external influences through the evening transition. *Q. J. R. Meteorol. Soc.* **2017**, *143*, 423–438. [CrossRef]
13. Liu, R.; Han, Z.; Li, J.; Li, J.; Liang, L.; Wu, Y. The impacts of urban anthropogenic heat and surface albedo change on boundary layer meteorology and air pollutants in the Beijing-Tianjin-Hebei region. *Urban Clim.* **2023**, *47*, 101358. [CrossRef]
14. Whiteman, C.D.; Zhong, S. Downslope flows on a low-angle slope and their interactions with valley inversions. Part I: Observations. *J. Appl. Meteorol. Climatol.* **2008**, *47*, 2023–2038. [CrossRef]
15. Darby, L.S.; Allwine, K.J.; Banta, R.M. Nocturnal low-level jet in a mountain basin complex. Part II: Transport and diffusion of tracer under stable conditions. *J. Appl. Meteorol. Climatol.* **2006**, *45*, 740–753. [CrossRef]
16. Jiang, Q.; Doyle, J.D. Diurnal variation of downslope winds in Owens Valley during the Sierra Rotor Experiment. *Mon. Weather Rev.* **2008**, *136*, 3760–3780. [CrossRef]
17. Savage III, L.C.; Zhong, S.; Yao, W.; Brown, W.J.; Horst, T.W.; Whiteman, C.D. An observational and numerical study of a regional-scale downslope flow in northern Arizona. *J. Geophys. Res. Atmos.* **2008**, *113*, D14114. [CrossRef]
18. Charrondière, C.; Brun, C.; Sicart, J.-E.; Cohard, J.-M.; Biron, R.; Blein, S. Buoyancy effects in the turbulence kinetic energy budget and Reynolds stress budget for a katabatic jet over a steep alpine slope. *Bound.-Layer Meteorol.* **2020**, *177*, 97–122. [CrossRef]
19. Stiperski, I.; Holtslag, A.A.; Lehner, M.; Hoch, S.W.; Whiteman, C.D. On the turbulence structure of deep katabatic flows on a gentle mesoscale slope. *Q. J. R. Meteorol. Soc.* **2020**, *146*, 1206–1231. [CrossRef]
20. Oldroyd, H.J.; Katul, G.; Pardyjak, E.R.; Parlange, M.B. Momentum balance of katabatic flow on steep slopes covered with short vegetation. *Geophys. Res. Lett.* **2014**, *41*, 4761–4768. [CrossRef]
21. Arrillaga, J.A.; Yagüe, C.; Román-Cascón, C.; Sastre, M.; Jiménez, M.A.; Maqueda, G.; Vilà-Guerau de Arellano, J. From weak to intense downslope winds: Origin, interaction with boundary-layer turbulence and impact on CO_2 variability. *Atmos. Chem. Phys.* **2019**, *19*, 4615–4635. [CrossRef]
22. Wenta, M.; Cassano, J.J. The atmospheric boundary layer and surface conditions during katabatic wind events over the Terra Nova Bay polynya. *Remote Sens.* **2020**, *12*, 4160. [CrossRef]
23. Elvidge, A.D.; Renfrew, I.A. The causes of foehn warming in the lee of mountains. *Bull. Am. Meteorol. Soc.* **2016**, *97*, 455–466. [CrossRef]
24. Sharples, J.J.; Mills, G.A.; McRae, R.H.; Weber, R.O. Foehn-like winds and elevated fire danger conditions in southeastern Australia. *J. Appl. Meteorol. Climatol.* **2010**, *49*, 1067–1095. [CrossRef]
25. Henao, J.J.; Mejia, J.F.; McDonough, F. Impacts of anthropogenic aerosols on orographic precipitation in Arizona. *Urban Clim.* **2023**, *49*, 101561. [CrossRef]
26. Abatzoglou, J.T.; Hatchett, B.J.; Fox-Hughes, P.; Gershunov, A.; Nauslar, N.J. Global climatology of synoptically-forced downslope winds. *Int. J. Climatol.* **2021**, *41*, 31–50. [CrossRef]
27. Shestakova, A.A.; Toropov, P.A.; Matveeva, T.A. Climatology of extreme downslope windstorms in the Russian Arctic. *Weather Clim. Extrem.* **2020**, *28*, 100256. [CrossRef]
28. Takimoto, I. Case study of the downslope wind of Japan "Rokko-oroshi". *Atmos. Sci. Lett.* **2022**, *23*, e1097. [CrossRef]
29. Elshora, M.; Xia, H.; Su, L.; Wei, T. Observation and study of consecutive dust storms in the Taklimakan desert from March 16 to 27, 2022, using reanalysis models and lidar. *Atmos. Res.* **2024**, *305*, 107431. [CrossRef]
30. Jin, L.; He, Q.; Li, Z.; Deng, M.; Abbas, A. Variation characteristics of dust in the Taklimakan Desert. *Nat. Hazards* **2024**, *120*, 2129–2153. [CrossRef]
31. Yang, X.; Shen, S.; Yang, F.; He, Q.; Ali, M.; Huo, W.; Liu, X. Spatial and temporal variations of blowing dust events in the Taklimakan Desert. *Theor. Appl. Climatol.* **2016**, *125*, 669–677. [CrossRef]
32. Bell, B.; Hersbach, H.; Simmons, A.; Berrisford, P.; Dahlgren, P.; Horányi, A.; Muñoz-Sabater, J.; Nicolas, J.; Radu, R.; Schepers, D. The ERA5 global reanalysis: Preliminary extension to 1950. *Q. J. R. Meteorol. Soc.* **2021**, *147*, 4186–4227. [CrossRef]
33. Huang, J.; Yin, J.; Wang, M.; He, Q.; Guo, J.; Zhang, J.; Liang, X.; Xie, Y. Evaluation of five reanalysis products with radiosonde observations over the Central Taklimakan Desert during summer. *Earth Space Sci.* **2021**, *8*, e2021EA001707. [CrossRef]
34. Tong, B.; Guo, J.; Wang, Y.; Li, J.; Yun, Y.; Solanki, R.; Hu, N.; Yang, H.; Li, H.; Su, J. The near-surface turbulent kinetic energy characteristics under the different convection regimes at four towers with contrasting underlying surfaces. *Atmos. Res.* **2022**, *270*, 106073. [CrossRef]

35. Yuan, J.; Su, L.; Xia, H.; Li, Y.; Zhang, M.; Zhen, G.; Li, J. Microburst, windshear, gust front, and vortex detection in mega airport using a single coherent Doppler wind lidar. *Remote Sens.* **2022**, *14*, 1626. [CrossRef]
36. Jiang, P.; Yuan, J.; Wu, K.; Wang, L.; Xia, H. Turbulence detection in the atmospheric boundary layer using coherent Doppler wind lidar and microwave radiometer. *Remote Sens.* **2022**, *14*, 2951. [CrossRef]
37. Wang, N.; Zhang, Y. Long-term variations of global dust emissions and climate control. *Environ. Pollut.* **2024**, *340*, 122847. [CrossRef]
38. Stull, R.B. *Practical Meteorology: An Algebra-Based Survey of Atmospheric Science*; University of British Columbia: Vancouver, BC, Canada, 2015.
39. Doran, J.; Horst, T.; Whiteman, C.D. The development and structure of nocturnal slope winds in a simple valley. *Bound.-Layer Meteorol.* **1990**, *52*, 41–68. [CrossRef]
40. Skyllingstad, E.D. Large-eddy simulation of katabatic flows. *Bound.-Layer Meteorol.* **2003**, *106*, 217–243. [CrossRef]
41. Park, J.-R.; Kim, J.-H.; Shin, Y.; Kim, S.-H.; Chun, H.-Y.; Jang, W.; Tsai, C.-L.; Lee, G. A numerical simulation of a strong windstorm event in the Taebaek Mountain Region in Korea during the ICE-POP 2018. *Atmos. Res.* **2022**, *272*, 106158. [CrossRef]
42. Turner, J.; Lu, H.; King, J.C.; Carpentier, S.; Lazzara, M.; Phillips, T.; Wille, J. An extreme high temperature event in coastal East Antarctica associated with an atmospheric river and record summer downslope winds. *Geophys. Res. Lett.* **2022**, *49*, e2021GL097108. [CrossRef]
43. Clements, C.B.; Whiteman, C.D.; Horel, J.D. Cold-air-pool structure and evolution in a mountain basin: Peter Sinks, Utah. *J. Appl. Meteorol. Climatol.* **2003**, *42*, 752–768. [CrossRef]
44. Steinacker, R.; Whiteman, C.; Dorninger, M.; Pospichal, B.; Eisenbach, S.; Holzer, A.; Weihs, P.; Mursch-Radlgruber, E.; Baumann, K. A sinkhole field experiment in the Eastern Alps. *Bull. Am. Meteorol. Soc.* **2007**, *88*, 701–716. [CrossRef]
45. Barry, R.G. *Mountain Weather and Climate*; Cambridge University Press: Cambridge, UK, 2008.
46. Zhong, S.; Whiteman, C.D. Downslope flows on a low-angle slope and their interactions with valley inversions. Part II: Numerical modeling. *J. Appl. Meteorol. Climatol.* **2008**, *47*, 2039–2057. [CrossRef]
47. Bossert, J.E.; Cotton, W.R. Regional-scale flows in mountainous terrain. Part I: A numerical and observational comparison. *Mon. Weather Rev.* **1994**, *122*, 1449–1471. [CrossRef]
48. Bossert, J.E.; Cotton, W.R. Regional-scale flows in mountainous terrain. Part II: Simplified numerical experiments. *Mon. Weather Rev.* **1994**, *122*, 1472–1489. [CrossRef]
49. Weissmann, M.; Braun, F.J.; Gantner, L.; Mayr, G.J.; Rahm, S.; Reitebuch, O. The Alpine mountain–plain circulation: Airborne Doppler lidar measurements and numerical simulations. *Mon. Weather Rev.* **2005**, *133*, 3095–3109. [CrossRef]
50. Sasaki, T.; Wu, P.; Mori, S.; Hamada, J.I.; Tauhid, Y.I.; Yamanaka, M.D.; Sribimawati, T.; Yoshikane, T.; Kimura, F. Vertical moisture transport above the mixed layer around the mountains in western Sumatra. *Geophys. Res. Lett.* **2004**, *31*, L08106. [CrossRef]
51. Bailey, S.C.; Smith, S.W.; Sama, M.P.; Al-Ghussain, L.; Boer, G.d. Shallow katabatic flow in a complex valley: An observational case study leveraging uncrewed aircraft systems. *Bound.-Layer Meteorol.* **2023**, *186*, 399–422. [CrossRef]
52. Nadeau, D.F.; Pardyjak, E.R.; Higgins, C.W.; Huwald, H.; Parlange, M.B. Flow during the evening transition over steep Alpine slopes. *Q. J. R. Meteorol. Soc.* **2013**, *139*, 607–624. [CrossRef]
53. Zhang, C.; Wang, Q.; Chan, P.W.; Li, Y. Potential "downstream blocking" synergistic mechanism for urban warming in Kowloon Peninsula, Hong Kong. *Urban Clim.* **2023**, *49*, 101517. [CrossRef]
54. Zhang, C.; Wang, Q.; Chan, P.W.; Li, Y. Performance of summertime temperature and wind fields under different background winds in Kowloon, Hong Kong. *Urban Clim.* **2023**, *49*, 101444. [CrossRef]
55. Evan, A.T. Downslope winds and dust storms in the salton basin. *Mon. Weather Rev.* **2019**, *147*, 2387–2402. [CrossRef]
56. Pokharel, A.K.; Kaplan, M.L.; Fiedler, S. Subtropical dust storms and downslope wind events. *J. Geophys. Res. Atmos.* **2017**, *122*, 10,191–10,205. [CrossRef]
57. Carvalho, L.; Duine, G.-J.; Jones, C.; Zigner, K.; Clements, C.; Kane, H.; Gore, C.; Bell, G.; Gamelin, B.; Gomberg, D. The sundowner winds experiment (SWEX) pilot study: Understanding downslope windstorms in the Santa Ynez Mountains, Santa Barbara, California. *Mon. Weather Rev.* **2020**, *148*, 1519–1539. [CrossRef]
58. Bi, J.; Li, Z.; Zuo, D.; Yang, F.; Li, B.; Ma, J.; Huang, Z.; He, Q. Dust aerosol vertical profiles in the hinterland of Taklimakan Desert during summer 2019. *Front. Environ. Sci.* **2022**, *10*, 851915. [CrossRef]
59. Dong, Q.; Huang, Z.; Li, W.; Li, Z.; Song, X.; Liu, W.; Wang, T.; Bi, J.; Shi, J. Polarization lidar measurements of dust optical properties at the junction of the Taklimakan Desert–Tibetan Plateau. *Remote Sens.* **2022**, *14*, 558. [CrossRef]